Research Square

Preprints are preliminary reports that have not undergone peer review.
They should not be considered conclusive, used to inform clinical practice,
or referenced by the media as validated information.

Analysis of Cavitation Flow and Energy Characteristics of Space Micro Pump under a Wide Temperature Range

Chuanchao Wang

wangchuanchaohit@163.com

Harbin Institute of Technology School of Energy Science and Engineering

Deyou Li

Harbin Institute of Technology School of Energy Science and Engineering

Qi Yang

Harbin Institute of Technology School of Energy Science and Engineering

Zhiwei Liu

Harbin Institute of Technology School of Energy Science and Engineering

Xiaolong Fu

Harbin Institute of Technology School of Energy Science and Engineering

Jintao Liu

Beijing Institute of Control Engineering

Zhipeng Ren

Harbin Institute of Technology School of Energy Science and Engineering

Research Article

Keywords: wide temperature range, space micro pump, cavitation flow, thermodynamic effect, hydraulic loss

Posted Date: March 13th, 2026

DOI: https://doi.org/10.21203/rs.3.rs-8973167/v1

License: This work is licensed under a Creative Commons Attribution 4.0 International License.
Read Full License

Analysis of Cavitation Flow and Energy Characteristics of Space Micro Pump under a Wide Temperature Range

Chuanchao Wang, M.Sc, School of Energy Science and Engineering, Harbin Institute of Technology, Harbin 150001, Heilongjiang, China
Email: wangchuanchaohit@163.com

Deyou Li, Professor, School of Energy Science and Engineering, Harbin Institute of Technology, Harbin 150001, Heilongjiang, China
Zhengzhou Research Institute, Harbin Institute of Technology, Zhengzhou 450000, Henan, China
Email: lideyou@hit.edu.cn
Corresponding author

Qi Yang, Ph D, School of Energy Science and Engineering, Harbin Institute of Technology, Harbin 150001, Heilongjiang, China
Email: yangqihit2021@163.com

Zhiwei Liu, Ph D, School of Energy Science and Engineering, Harbin Institute of Technology, Harbin 150001, Heilongjiang, China
Email: zwliu09@126.com

Xiaolong Fu, Associate Professor, School of Energy Science and Engineering, Harbin Institute of Technology, Harbin 150001, Heilongjiang, China
Email: fuxiaolong@hit.edu.cn

Jintao Liu, Senior Engineer, Beijing Institute of Control Engineering, Beijing, 100094, China
Email: ljt86@zju.edu.cn

Zhipeng Ren, Ph D, School of Energy Science and Engineering, Harbin Institute of Technology, Harbin 150001, Heilongjiang, China
Email: renzhipenghit@163.com

Abstract

The space micro pump has a wide temperature range, and it experiences obvious thermodynamic effects during the high-temperature cavitation process, which leads to complex flow characteristics. To evaluate the influence of different temperatures on the cavitation flow within the space micro pump, the shear-stress transport *k-ω* turbulence model (SST *k-ω*) and the Zwart-Gerbera-Belamri cavitation model (ZGB) corrected based on thermodynamic effects were used to conduct numerical simulations of the flow channels within the space micro pump. The physical parameters were coupled with temperature to study the cavitation flow in the space micropump over a wide temperature range, and the influence of the wide temperature range on cavitation flow was revealed. The results showed that at high temperatures, the thermodynamic effects manifested as a reduction in the saturated vapor pressure of the cavitation region, a delay in the development of cavitation cavities, a decrease in the vapor volume fraction, and a reduction in the negative impact of cavitation on the performance of micropumps owing to a decrease in viscosity at high temperatures. Moreover, the inhibitory effect of the thermodynamic effects did not increase simultaneously with an increase in temperature. Furthermore, cavitation increased flow losses, whereas following the temperature increase, cavitation inhibition and a decrease in viscosity worked together to reduce this loss.

Keywords: wide temperature range, space micro pump, cavitation flow, thermodynamic effect, hydraulic loss

Nomenclature

m^+	Evaporation source term	V	Volume of vapor, mm^3
m^-	Condensation source term	η	Efficiency, %
α_{nuc}	Vapor phase volume fraction of the non-condense	σ	Cavitation number
C_{vap}	Evaporation source term constant	U	Circumferential velocity of the impeller,m^3/s
C_{cond}	Condensation source term constant	n	Rotational speed, r/min
T	Temperature, K	P	Power output, W.
L_{ev}	Latent heat, $J \cdot kg^{-1}$	Re	Reynolds number
p_v	Saturated vapor pressure, pa	μ	Dynamic viscosity, Pa.s.
ρ	Density, $kg \cdot m^{-3}$	L_1	Length of inlet, mm.
g	Acceleration of gravity, kg/m^3	H	Head of the micropump, m
D_1	Outlet diameter of the impeller, mm	D_2	Inlet diameter of the impeller, mm
I	Hydraulic losses calculated by entropy production method, W	L	Characteristic length, m
γ	Surface tension coefficient	k	Turbulent kinetic energy,m^2/s^2

1. Introduction

With improvements in the functionality and complexity of spacecraft, there have been increases in the amount of heat generated by components and an associated demand for heat dissipation. A two-phase fluid-loop thermal control system is a future development direction; the space micropump is the core of this system, and its performance of the space micropump affects the operational lifespan of the spacecraft. Space micropumps are subjected to a harsh working environment characterized by a high operating temperature, wide temperature range, high head pressure, and frequent and significant temperature fluctuations. Aerodynamic cavitation is a complex flow phenomenon commonly observed in various rotating machineries, and problems caused by cavitation flows have attracted extensive research attention [1]. Cavitation can lead to a decline in pump performance, a decrease in efficiency, and the generation of vibration and noise, and may even damage components [2]. In addition, the cavitation phenomena at different temperatures have varying degrees of influence on the space micropump.

Traditional pump cavitation numerical simulation studies have primarily been based on the assumption of isothermal conditions. However, during the cavitation process, parameters such as the saturated vapor pressure of the working medium, change with temperature. Perfluorotriethylamine (PFTEA) is a new type of coolant that exhibits a wide temperature adaptability, chemical inertness, and low viscosity. A loop system was used as the circulating medium. However, their physical properties vary significantly over a wide range of operating temperatures. The thermodynamic effect is crucial for the numerical simulation accuracy of high-temperature cavitation flows [3]. Furthermore, intense unstable behavior occurs during the evolution of cavitation flow.

Studies have been conducted to analyze the cavitation characteristics of centrifugal pumps. In this respect, Tan et al. [5] introduced a filtering function to correct the vortex viscosity and adopted a full cavitation model. They found that in low-flow conditions in centrifugal pumps, with an increase in Net Positive Suction Head Available (H_{NPSHa}, the device cavitation margin), the cavitation cavities expanded towards the rim of the flow channel. Sun et al. [6] employed a Bubble-Rotation-based Zwart–Gerber–Belamri cavitation model (BRZGB) based on bubble rotation correction to investigate the interactions among cavitation, vortices, and pressure fluctuations in centrifugal pumps. In addition, Mousmoulis et al. [7] discovered that cavitation development is closely related to the recirculation between the impeller blades, and Wang et al. [8] employed a rotating-corrected Zwart–Gerber–Belamri cavitation model (RZGB) and discovered that the trailing edge region of attached cavitation cavities was prone to damage. Furthermore, Jia et al. [9] discovered that when cavitation fills a flow channel, the load pressure on the blades suddenly decreases, causing them to malfunction.

When studying the thermodynamic influence of cavitation flow, studies have considered the influence of thermodynamic effects on cavitation in different working fluids. Rakibuzzaman et al. [10] discovered that as the water temperature increased, the saturated vapor pressure increased and the degree of cavitation erosion on the centrifugal pump significantly intensified. Zhang et al. [11] discovered that in a high-speed centrifugal pump with a low-temperature thermosensitive fluid, the thermal effect significantly suppressed the development and collapse of cavitation through a local temperature reduction. Zhang et al. [12] discovered through a cavitation experiment using an 1,1,1,2-Tetrafluoroethane (R134a) high-speed centrifugal pump, that both the critical cavitation number and the desinent cavitation number increased as the temperature decreased, and the cavitation intensified. Liu et al. [13] discovered that an increase in the temperature of RP-3 aviation kerosene in an aircraft centrifugal fuel pump exacerbated cavitation. Furthermore, some studies have obtained accurate numerical simulation results using modified cavitation models. Zhang et al. [14] constructed a Zwart correction model based on the generation time of the thermal boundary layer and found that the size of the cavitation chamber and the volume fraction of vapor decreased significantly at high temperatures. Xu et al. [15] used the actual saturated vapor pressure and considered the thermodynamic effects to modify the evaporation and condensation source terms, thereby more accurately simulating the cavitation flow of a hydrofoil in a low-temperature medium. Furthermore, Tian [16] combined the B factor, characteristic temperature drop, and Clapeyron equation to develop a modified ZGB cavitation model and achieve results that were in good agreement with the experiments. The influence of the thermodynamic effects on cavitation varies significantly depending on the working fluid and temperature range.

A space micropump operates in a microgravity environment, where surface tension takes over the dominant role previously played by gravity. Surface tension prevents the bubbles from separating and inhibits their expansion. Sunjae et al. [17] conducted an experimental study of the boiling of liquid

nitrogen in a microgravity environment and found that the surface tension maintained a stable distribution of bubbles. Agarwal et al. [18] demonstrated that the Volume of Fluid two-phase flow model (VOF) can be applied to the numerical simulation of gas-liquid two-phase flows under microgravity conditions. Zhu et al. [19] conducted a microgravity drop tower experiment and showed that under microgravity conditions, the contact angle was 10–20 ° smaller than that under normal gravity. In addition, Mousavi et al. [20] discovered that, under microgravity conditions, an increase in the wall contact angle reduced the curvature radius of the convex surface of the bubble and increased its length.

In recent years, entropy generation theory has been used to quantify hydraulic losses in fluid machinery to determine their distribution and sources. The growth and collapse of cavitation cavities, vortices, and recirculation was found to affect energy conversion and transmission [21]. Li et al. [22] analyzed a hydrofoil and found that the main areas for the local entropy production rate generated by the velocity gradient (EPRV) were at the end of the cavity and tail of the hydrofoil. Yu et al. [23] discovered that the local entropy production rate generated by the temperature gradient (EPRT) in a hydrofoil cavitation flow was lower than that in an EPRV, and Wang et al. [25] indicated that the intensification of cavitation significantly increases the entropy production in the impeller. Furthermore, Lai et al. [26] found that in cavitation flow within a centrifugal pump, the rapid decrease in the head is mainly attributed to the rapid increase in the entropy generation rate near the wall at the pressure surface of the blade and the blade trailing edge.

The aforementioned studies on cavitation flow have provided a deeper understanding of cavitation flow within microcentrifugal pumps. However, most of these studies either did not consider the influence of thermodynamic effects on cavitation, the studied temperature range was limited, or they did not consider hydraulic losses to obtain more detailed thermodynamic characteristics. Furthermore, different results have been obtained in studies of the thermal effects on cavitation from the use of various working fluids. It is acknowledged that the influence of thermal effects on the cavitation of PFTEA over a wide temperature range may differ significantly from the results for the aforementioned working fluid (such as water), but very few studies have focused on cavitation associated with the working fluid PFTEA.

Therefore, this study focused on analyzing the performance of space micropumps under harsh conditions and the impact of thermodynamic effects on the cavitation flow. First, a modified cavitation model considering thermodynamic effects was established to simulate the entire flow field of a space micropump. Second, under a wide temperature range of -20 ℃ to 72 ℃, the specific effects of cavitation phenomena at different temperatures were investigated, and the influence of temperature on various hydraulic losses in the cavitation flow of space micro pumps was analyzed based on entropy production theory.

2. Numerical modeling and schemes

2.1. Computational models and grid generation

The geometric structure of the space micropump model is presented in Table 1. The total fluid domain consists of three parts: the inlet, impeller, and volute domains. The overall configuration was realized using UG software. The entire computational domain of the space micropump is shown in Fig. 1. It was divided into hexahedral mesh elements, and the mesh quality of each domain was not less than 0.2. The mesh details are shown in Fig. 2. The blade grid was further refined to satisfy the requirements of the selected turbulence and capture the detailed flow on the wall.

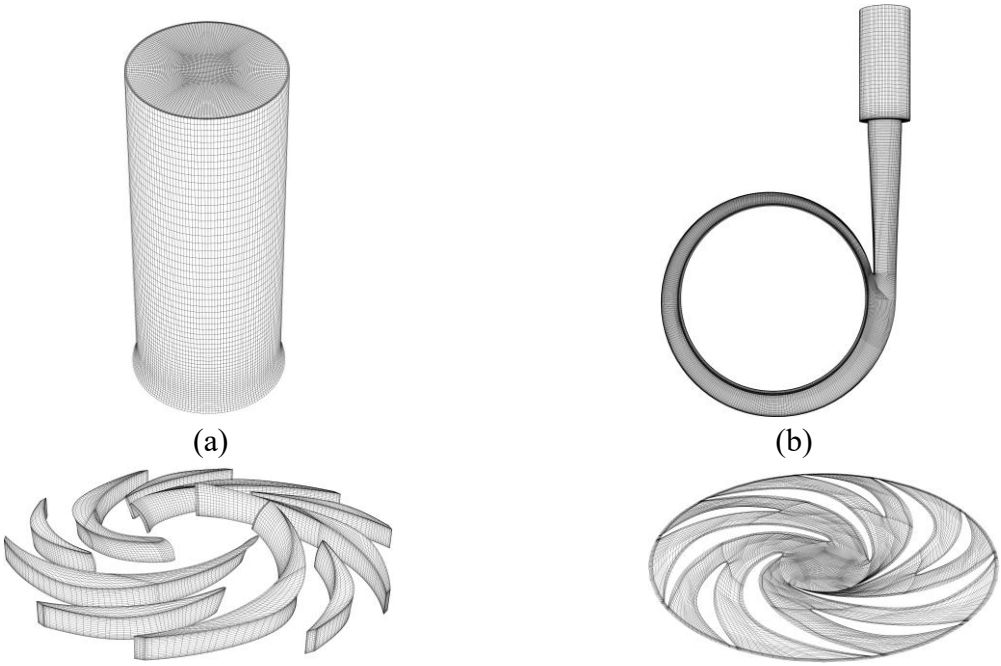
Table 1 Key micropump parameters.

Geometric parameter	Value
Length of the pump inlet section L_1(mm)	15.0
Number of short blades (-)	5
Number of long blades (-)	5
Diameter of the impeller outlet D_1 (mm)	22.4
Diameter of the impeller inlet D_2 (mm)	6.6



(a) (b)

Fig. 1. Computational configuration



(a) (b)

(c) (d)

Fig. 2. Micropump grid details

2.2. Basic equations and cavitation models

Cavitation is a multi-phase flow problem. In a microgravity environment, the bubbles formed are mainly influenced by the inertial force and surface tension, and the effect of the latter cannot be ignored under microgravity conditions. The VOF method can be employed to reveal the influence of surface tension by tracking the phase interface. The VOF method [27] was therefore adopted to simulate the microgravity environment, and the Navier-Stokes equation is as follows,

$$\frac{\partial \phi}{\partial t} + u \cdot \nabla \phi = 0 \,, \tag{1}$$

$$\frac{\partial(\rho_m u_i)}{\partial t} + \frac{\partial(\rho_m u_i u_j)}{\partial x_j} = -\frac{\partial p}{\partial x_i} + \frac{\partial}{\partial x_j}[(\mu + \mu_t)(\frac{\partial u_i}{\partial x_j} + \frac{\partial u_j}{\partial x_i})] + \gamma \kappa \delta(d) n_i \,, \tag{2}$$

where t represents time, $\rho_m = \rho_1(1-\alpha_v) + \rho_v \alpha_v$ represents the density of the mixed medium (ρ_l is the density of the liquid, and ρ_v and α_v are the density and volume fraction of the vapor, respectively), and x_j and u_j are the velocity components in the Cartesian coordinate system and the coordinate system, respectively. The last item represents the surface tension concentrated at the interface: γ is the surface tension coefficient; κ is the curvature of the phase interface; d is the vertical distance of the point in the calculation area from the phase interface; n is the unit vector normal to the phase interface pointing outward; and δ is the Dirac Delta function.

The surface-tension model in Fluent is a continuous surface-force model. The additional surface tension variation in the VOF calculations is represented by the surface tension coefficient. In this study, the surface tension coefficients of PFTEA at various temperatures were determined by referring to tables,

and the surface tension coefficients corresponding to the temperatures at each point were obtained through polynomial fitting.

$$\gamma=0.033584-7.6817T \tag{3}$$

In this study, to consider thermodynamic effects, the energy equation was solved during the simulation process, as shown in Equation (4),

$$\frac{\partial}{\partial t}[\rho_m h_{tot}]-\frac{\partial p}{\partial t}+\frac{\partial}{\partial x_j}\left[\rho_m u_j h_{tot}\right]=\nabla\cdot(k_{eff}\nabla T)+\nabla\cdot(U\cdot\tau)+S_E, \tag{4}$$

where h_{tot} represents total enthalpy, h is static enthalpy, k_{eff} is effective thermal conductivity, $\nabla\cdot(U\cdot\tau)$ represents the work done by viscous stress, and S_E is the energy source term, which was included to consider phase-change heat transfer in the cavitation simulation.

To accurately simulate the flow field characteristics within the rotating channel between the impeller and the volute, the shear stress transport SST k-ω model [28] was adopted.

The ZGB cavitation model, derived from the Rayleigh-Plesset equation, was adopted to predict the cavitation process of the space micropump. The two-phase transition is usually represented by the evaporation ($\dot{m}^+$) and condensation ($\dot{m}^-$) source terms, which are expressed as follows,

$$\dot{m}^+=C_{vap}\frac{3\alpha_{nuc}(1-\alpha_v)\rho_v}{R_B}\sqrt{\frac{2}{3}\frac{(p_v-p)}{\rho_l}}(p,, p_v), \tag{5}$$

$$\dot{m}^-=C_{cond}\frac{3\alpha_v\rho_v}{R_B}\sqrt{\frac{2}{3}\frac{(p-p_v)}{\rho_l}}(p\geq p_v), \tag{6}$$

where α_{nuc} ($\alpha_{nuc}=5\times10^{-4}$) represents the volume fraction of the gas phase in the non-condensing phase, and $R_B=1\times10^{-6}$m. C_{vap} and C_{cond} are constants of the evaporation and condensation source terms, respectively, and they depend only on the medium type. However, when the liquid evaporates, heat is absorbed by the surrounding liquid, resulting in a local decrease in temperature. The pressure value drops to P_v (T), where T is the current temperature inside the cavitation cavity, and the temperature difference is ΔT. Considering the influence of the turbulent kinetic energy and thermodynamic effects on the bubble pressure, the internal bubble pressure is corrected as follows,

$$p^*(T)=p_v(T)+\Delta p_{\text{turb}}=p_v(T_\infty)-\Delta p_{\text{v}}+\Delta p_{\text{turb}}. \tag{7}$$

In addition, the influence of the change in turbulent kinetic energy on the cavitation cavity pressure is,

$$\Delta p_{\text{turb}}=0.195\rho_{\text{m}}k. \tag{8}$$

Compared with the saturated vapor pressure corresponding to the mainstream temperature, ΔP_v. is the change in saturated vapor pressure caused by the temperature drop. Through Taylor series expansion, ΔP_v can be regarded as the product of the first-order derivative term and the temperature difference term, which is employed to obtain the functional relationship between the pressure change and the temperature change,

$$\Delta p_{\text{v}}=p_v(T_\infty)-p_v(T)\approx\frac{\mathrm{d}p_v}{\mathrm{d}T}\Delta T. \tag{9}$$

Based on the heat balance equation for the vapor-liquid two-phase system [29], the temperature drop can be estimated using the physical properties of the vapor-liquid two-phase system after transformation,

$$\rho_v v_v L_{ev}=\rho_l v_l C_{pl}\Delta T. \tag{10}$$

Furthermore, the characteristic temperature drop when the fluid in a unit volume changes from the liquid to vapor phase is expressed as follows,

$$\Delta T^*=\frac{\rho_v L_{ev}}{\rho_l C_{pl}}. \tag{11}$$

To characterize the relationship between the temperature drop during cavitation and the intensity of the phase transition between gas and liquid, the B factor and characteristic temperature drop are introduced

[30]. The temperature drop expression with the two-phase thermal properties and vapor-phase volume fraction as variables is as follows,

$$\Delta T = B\Delta T^* = \frac{\alpha_v}{1-\alpha_v}\frac{\rho_v L_{ev}}{\rho_l C_{pl}}. \tag{12}$$

The Clapeyron equation is used to describe the rate at which pressure changes with temperature during the phase transition process. The density of steam can be considered negligible compared to that of the liquid. Therefore,

$$\frac{L_{ev}}{T} = (\frac{dp_v}{dT})\left(\frac{1}{\rho_v}-\frac{1}{\rho_l}\right) \approx (\frac{dp_v}{dT})\frac{1}{\rho_v}. \tag{13}$$

As such, the expression for the first-order derivative term is obtained,

$$\frac{dp_v}{dT} = \frac{\rho_v L_{ev}}{T}. \tag{14}$$

By combining Equations (9) and (13), the pressure change caused by the temperature drop can be derived as follows,

$$\Delta p_v = p_v(T_\infty) - p_v(T) \approx \frac{\mathrm{d}p_v}{\mathrm{d}T}\Delta T = \frac{\alpha_v {L_{ev}}^2 \rho_v^2}{\rho_1 C_{pl} T\left(1-\alpha_v\right)}. \tag{15}$$

The evaporation source term $\dot{m}^+$ and condensation source term $\dot{m}^-$ of the ZGB cavitation model corrected based on the change in the internal pressure of the cavity are as follows [16],

$$\dot{m}^+ = C_{\mathrm{vap}}\frac{3\alpha_{\mathrm{nuc}}\left(1-\alpha_v\right)\rho_v}{R}\left(\sqrt{\frac{2}{3}\frac{p^*(T)-p}{\rho_l}}\right)(p \le p^*(T)), \tag{16}$$

$$\dot{m}^- = C_{\mathrm{cond}}\frac{3\alpha_v\rho_v}{R}\left(\sqrt{\frac{2}{3}\frac{p-p^*(T)}{\rho_l}}\right)(p \ge p^*(T)), \tag{17}$$

where $p^*(T) = p_v(T_\infty) - \frac{\alpha_v {L_{ev}}^2 \rho_v^2}{\rho_1 C_{pl} T\left(1-\alpha_v\right)} + 0.195\rho_m k_m$. In the correction equation, $p_v(T)$, ρ_l, ρ_v, and L_{ev} are related to temperature. Of these, $p_v(T)$ is applicable to the temperature of PFTEA within the range of 253.15 to 345.15 K. Furthermore,

$$\ln p_v = -70.34 + 0.7378T - 2.680\times10^{-2}T^2 + 4.648\times10^{-6}T^3 - 3.137\times10^{-9}T^4. \tag{18}$$

2.3. Numerical boundary conditions

The numerical simulation is based on ANSYS Fluent 2023R1. Three types of boundary conditions are required: inlet and outlet, and the wall and domain interfaces. Under the actual conditions, the reference pressure is 0 (Pa), and the inlet pressure is defined by the cavitation number formula, as shown in Equation (13). The outlet is set as a gradually increasing mass-flow outlet within the volute. The adiabatic condition (with no slip boundary) is applied to all surfaces. The gravitational acceleration is set to 10^{-3}g, and the contact angle correction is set to 80°. The cavitation number is defined as follows:

$$\sigma = \frac{p_\infty - p_v}{\frac{1}{2}\rho U^2} \tag{19}$$

where σ represents the cavitation number, U is the outer edge linear velocity of the blade, and p_∞ and p_v are the far-field static pressure and saturated vapor pressure, respectively.

2.4. Grid independence test

The number of grids significantly affects the numerical results. To determine the appropriate value, independent numerical simulations were conducted for the entire space-micropump calculation domain. Five sets of grids with different numbers of nodes (as shown in Table 2) were selected, along with the calculation temperature (20℃), rotational speed (8000 rpm), and the working fluid (PFTEA), including the head. Due to the current difficulty in conducting space micro-pump experiments under microgravity conditions, an external characteristic experiment was conducted on the micro-pump's operation at 20°C under normal gravity to verify the accuracy and validity of the numerical model used. The simulation results were in good agreement with the experimental results near the rated flow rate. Generally, the head obtained from the simulation is always higher than that obtained from the experiment because the simulation ignores possible flow losses that may occur, resulting in an increase in the head.

Table 2 Micropump grid details ($\times 10^4$).

Parts	Set1	Set2	Set3	Set4	Set5
Inlet	55.2	70.5	82.0	102.8	138.1
Impeller	55.7	86.9	148.8	188.7	260.0
Outlet	72.3	128.1	134.3	190.4	252.1
Total	183.2	285.5	365.1	481.9	650.2

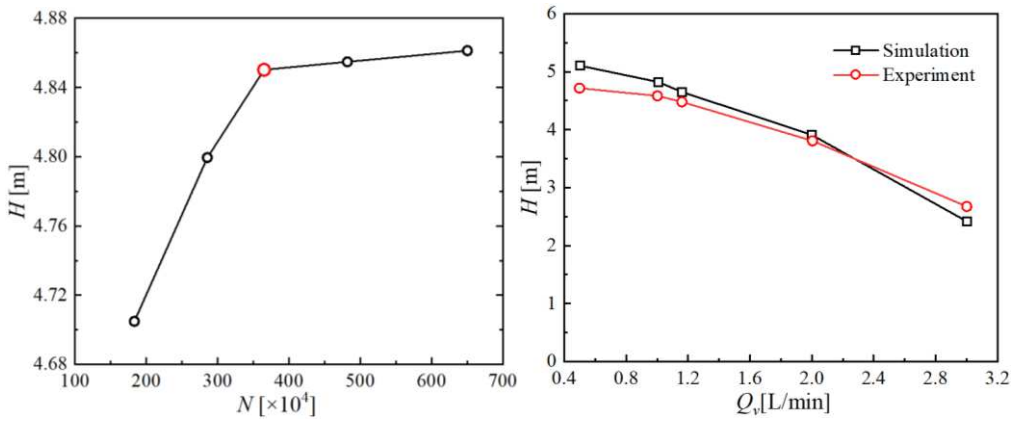


Fig. 3. Validation of mesh independence and comparison between experiment results and numerical calculations

3. Results and discussion

3.1 Comparative analysis of the impeller

Typically, space micropumps operate at rated flow rates within a certain temperature range. Therefore, the results below were calculated under the operating conditions of PFTEA at -20℃ to 72℃ and at a flow rate of 1.16 L/min. To verify the effect of cavitation on performance and hydraulic loss at different temperatures, numerical simulations were conducted in PFTEA for five temperatures (-20℃, 0℃, 25℃, 50℃, 72℃) at a rotational speed of 8000 rpm.

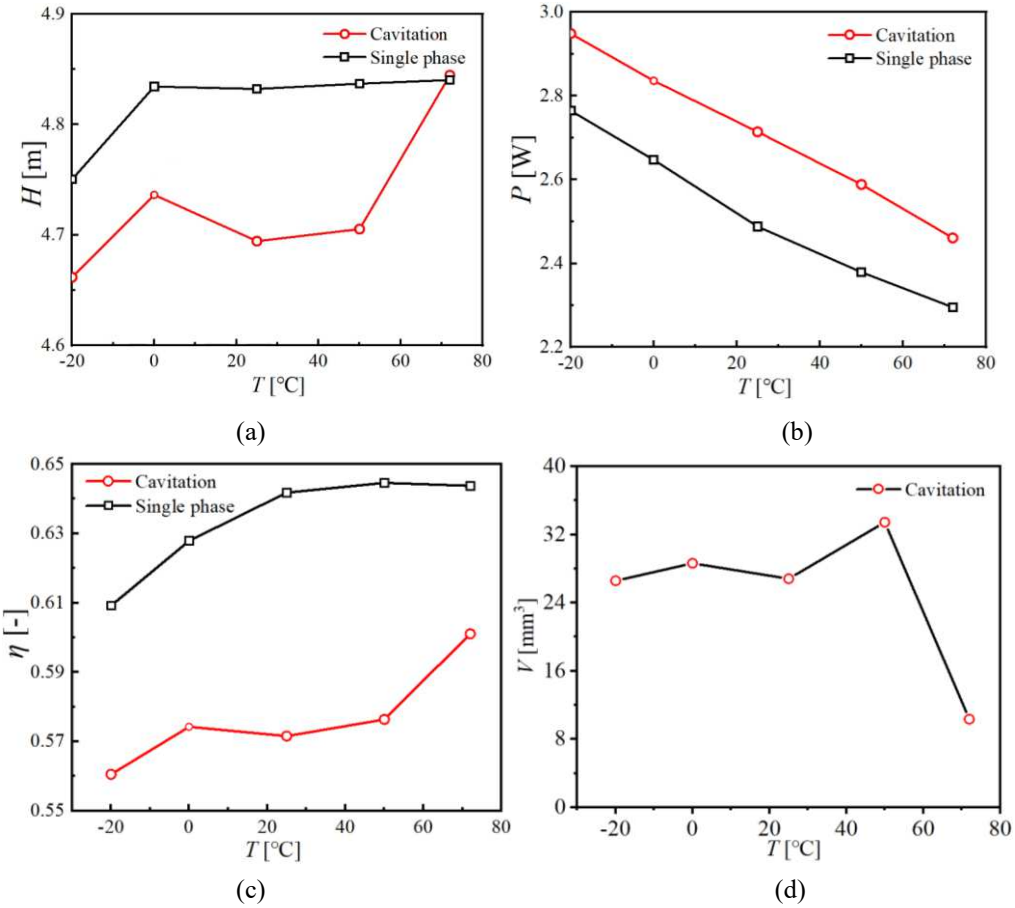


Fig. 4. Comparison of the external characteristics at different temperatures

Figure 4 shows the curves of head, shaft power, efficiency, and the volume of vapor change of the space micro pump centrifugal pump under rated flow conditions at different temperature conditions. As shown in Fig. 4(a), the head increased first and then stabilized with an increase in temperature. Cavitation caused head loss, which increased first and then decreased with the increase of temperature. The head decreased most significantly at 25℃ and 50℃ cavitation conditions, with a reduction of more than 3%. As shown in Fig. 4(b), the shaft power decreased gradually with increasing temperature. Cavitation increased the shaft power, and this increase was broadly similar at different temperatures, with an average increase of approximately 8%. As shown in Fig. 4(c), between -20℃ and 72℃, the rate of increase in efficiency slowed as the temperature rose. Cavitation caused a significant decrease in the efficiency under low-temperature conditions, with an average reduction of more than 10%, and the declining trend was weakened under high-temperature conditions. As shown in Fig. 4(d), the volume of vapor gradually increased between -20℃ and 50℃, and then dropped sharply between 50℃ and 72℃.

The head, shaft power, and efficiency were significantly affected by the volume of the vapor and viscosity of the liquid. The existence of cavitation cavities blocked the flow channels inside the impeller, hindered liquid flow, and increased the local resistance loss. Therefore, as the head decreased, the shaft power increased, and under the combined influence of these two factors, the efficiency significantly decreased. At high temperatures, the flow resistance decreased as the viscosity of the liquid decreased and cavitation weakened.

3.2. Comparative analysis of impeller

The distribution of the cavitation inside the space micropump at different temperatures is shown in Fig. 6.

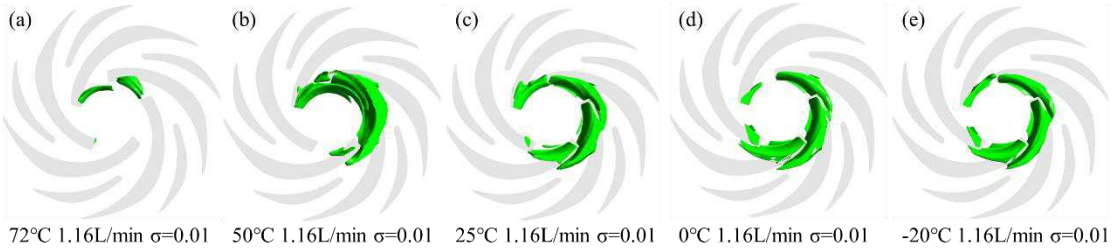


Fig. 5. Distribution of cavitation region at different temperatures

The cavitation region is represented by an isosurface with a volume fraction of 0.5. At 20℃, as shown in Fig. 5(e), the cavitation cavities were distributed on the back side of the long blade inlet end and formed an annular shape. The volume of the cavitation cavities was large and the shape was relatively regular; as the temperature increased, the cavitation region became more concentrated, but there was little change in the total volume of the bubbles. When the temperature increased to 50℃ (Fig. 5b), the total volume of the cavitation cavities significantly increased, the shape became irregular, and the boundary burrs and protrusions increased. When the temperature rose to 72℃ (Fig. 5a), the total volume of the cavitation rapidly decreased, the cavitation region shrank significantly, and cavitation was significantly suppressed. With increasing temperature, the thermodynamic effect strengthened, significantly suppressing cavitation and reducing the bubble volume.

To understand the complex flow phenomena within the impeller, the flow conditions at the middle of the flow face were studied. For the position of the flow face, please see Fig.1(b).

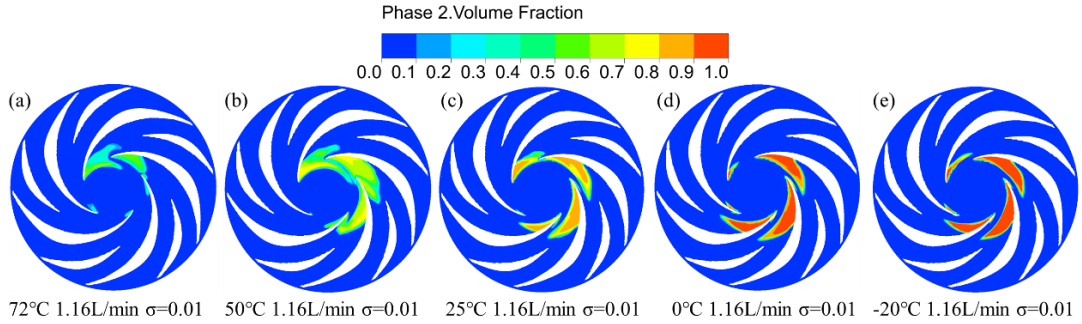


Fig. 6. Distribution of vapor volume fraction at different temperatures

The distribution characteristics and variation patterns of the vapor volume fraction at different temperatures are presented in Fig. 6. As shown in Figures 6(d) and 6(e), at low temperatures, the cavitation core was mainly located in the low-pressure area of the blades. In particular, on the back side of the blades, the cavitation areas were scattered and irregularly distributed, the boundaries were the clearest, and the volume fraction changed dramatically. As shown in Figures 6(b) and 6(c), with an increase in temperature, the cavitation areas were concentrated on some of the blades, presenting a ring-like distribution. The cavitation region expanded, and its boundary became less distinct. The peak volume fraction gradually decreased. As shown in Fig. 6(a), at high temperatures, the volume fraction changed more gradually, the boundaries blurred, and the cavitation areas shrank sharply. Under high-temperature conditions, the liquid was more likely to reach the cavitation condition, but the thermodynamic effect also inhibited cavitation development and bubble development was suppressed, resulting in a decrease in the vapor volume fraction. The suppressive effect of the thermodynamic effect on cavitation did not increase proportionally with increasing temperature.

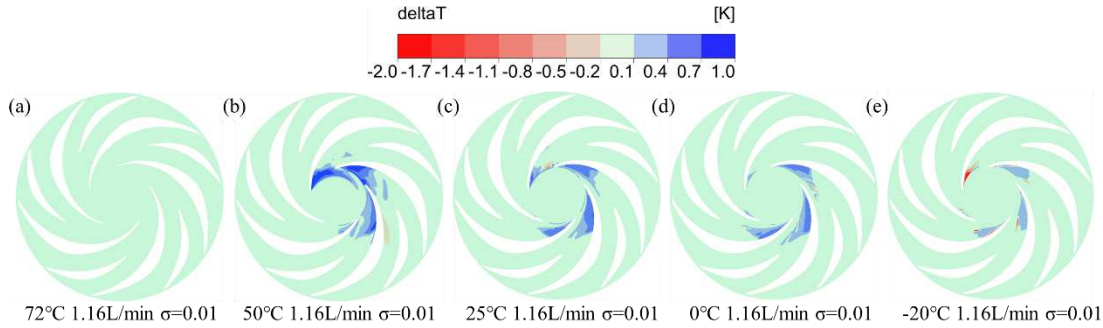


Fig. 7. Distribution of temperature drop at different temperatures

Contour plots of the vapor volume fraction and its variation patterns at different temperatures are shown in Fig. 7. In Fig. 7(e), the temperature within the cavitation region decreased owing to heat absorption during fluid vaporization, whereas the temperature at the tail of the cavitation cavities increased owing to the heat released from vapor condensation. As shown in Figs. 7(d), (c), and (b), as the temperature increased, the temperature drop in the cavitation region became more pronounced, whereas the temperature rise at the tail of the cavitation cavities weakened. The most significant temperature drop within the cavitation region occurred at 50℃. In Fig. 7(a) at 72℃, the thermodynamic effect strongly suppressed cavitation development, resulting in virtually no temperature change in the cavitation region.

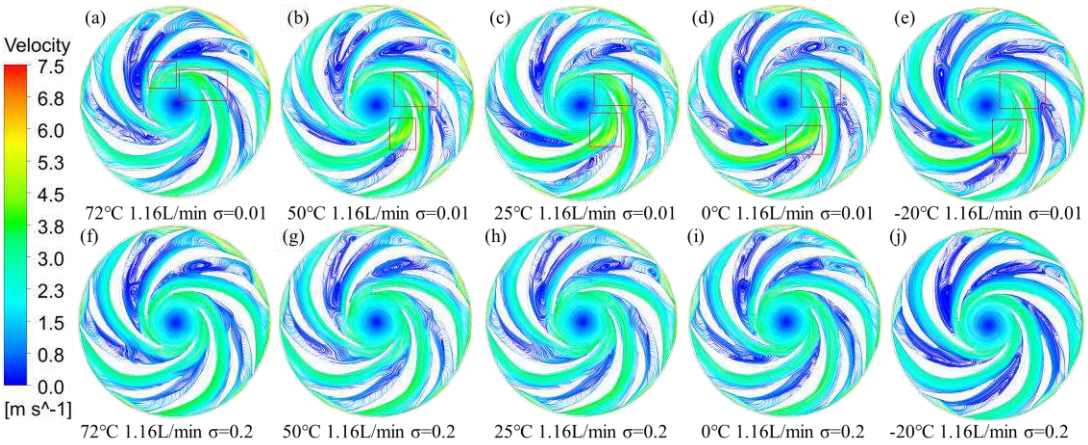


Fig. 8. Distribution of streamline at different temperatures

Figure 8 shows the streamline distributions at different temperatures and cavitation numbers. As shown in Fig. 8(j), without cavitation, the streamline distributions at the back side and working surface of the long-blade inlet were uniform. At low temperatures, stable large-scale vortices were formed in the rear flow channel of the long blade, and a clear recirculation zone was generated at the outer edge of the impeller. As shown in Fig. 8(f), as the temperature increased, the intensity of the vortex at the outer edge of the impeller weakened, and the recirculation boundary became blurred. The turbulence intensity primarily depends on the Reynolds number Re,

$$Re = \frac{\rho v L}{\mu} \tag{20}$$

where ρ represents the density of the fluid (kg/m³), v represents the velocity of the fluid (m/s), μ represents the dynamic viscosity (Pa·s), and L represents the characteristic length (m). The decrease in viscosity resulted in an increase in the Reynolds number with a corresponding increase in the turbulence intensity. In Fig. 8(e), during low-temperature cavitation, the fluid bypassed the cavitation cavities near the suction side of the leading edge of the blade (red-box region), causing local flow deflection. Downstream of the cavity collapse, the vortex activity intensified with significantly enlarged vortex structures. As shown in Figure 8(a), at high temperatures, the thermodynamic effect inhibited the

development of cavitation, resulting in a reduced streamline deviation and weakened vortex intensity. Cavitation affected the stability, by directly altering the velocity distribution of the flow field. As the temperature increased, the enhanced thermodynamic effect significantly suppressed cavitation, which manifested as delayed bubble development and constrained cavitation.

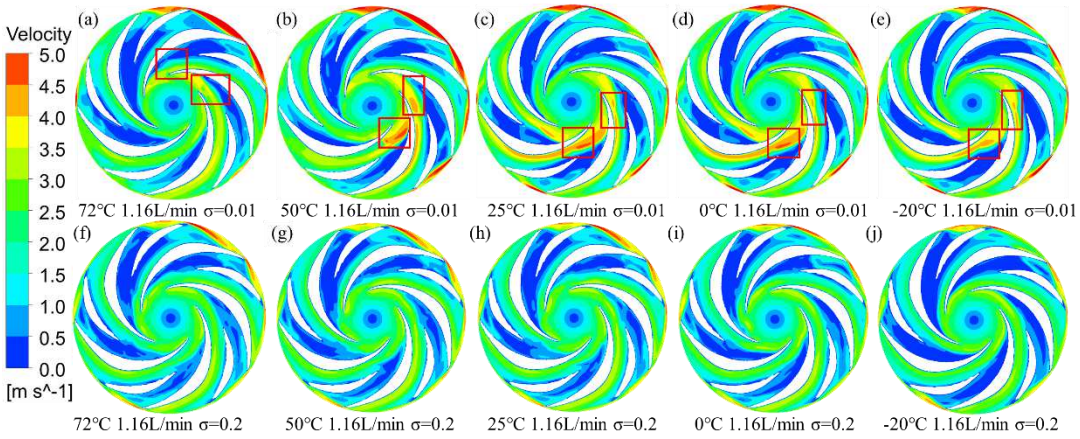


Fig. 9. Distribution of velocity at different temperatures

Figure 9 shows the velocity distributions at different temperatures and cavitation numbers. Significant variations emerged in the influence of cavitation on the local velocity profiles with increasing temperature. A comparison of Figs. 9(e) and 9(j) at low temperatures reveals that cavitation induced high-velocity zones through vapor cavity-induced flow constriction, resulting in abnormally steep velocity gradients. As the temperature increased to medium levels (Figs. 9c,b), the enhanced fluid displacement from the expanding cavities concurrently amplified the velocity gradients in this region. As shown in Fig. 9(a), under high-temperature cavitating conditions, the velocities in this region approached the noncavitating baseline values with significantly reduced gradients. The non-cavitating case at high temperatures exhibited the most uniform velocity distribution, demonstrating how reduced viscosity improved the flow-field uniformity.

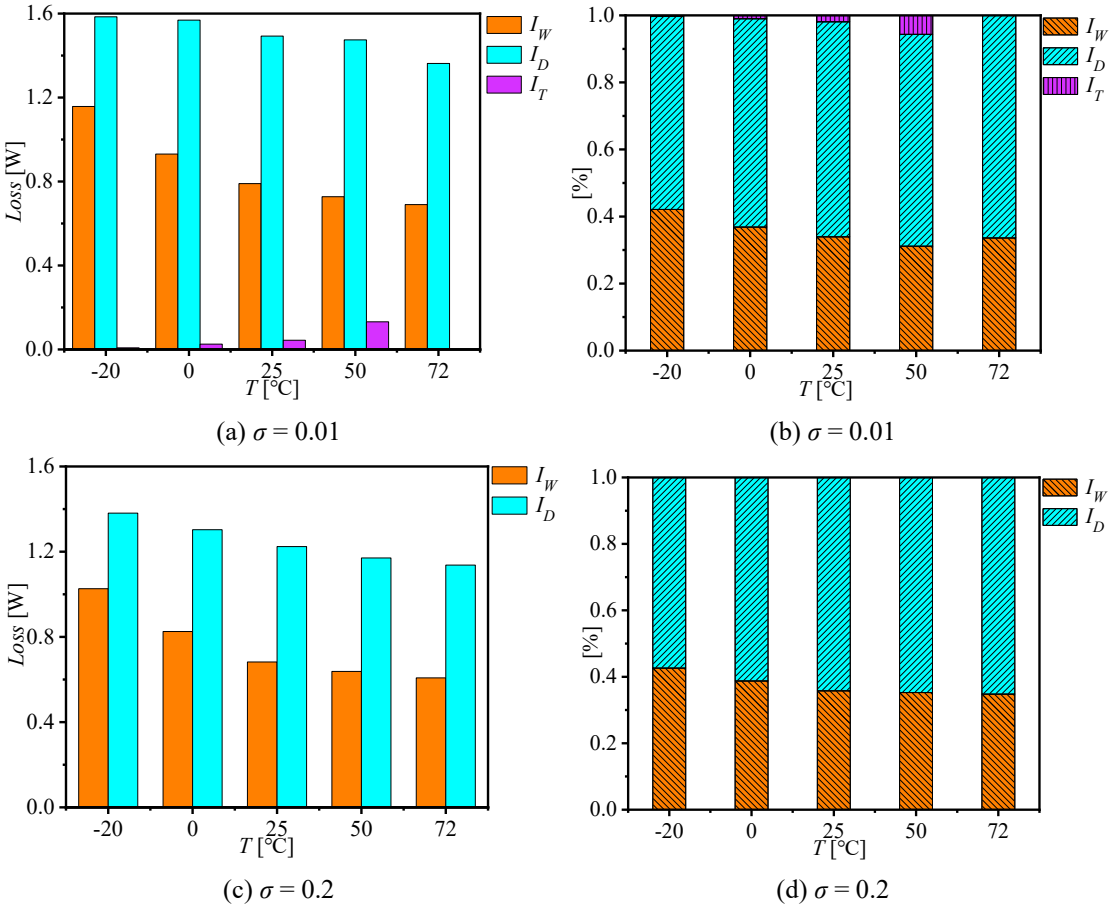
3.3. Analysis of hydraulic losses

Using entropy production theory for analysis, a quantitative evaluation of hydraulic losses was conducted to determine the spatial distribution of energy losses. The total hydraulic loss of a watershed system is expressed as (refer to [23] for details),

$$I = I_{\bar{D}} + I_{D'} + I_{\bar{T}} + I_{T'} + I_W, \tag{21}$$

where the energy loss caused by the velocity gradient is $I_D = I_{\bar{D}} + I_{D'}$, the energy loss caused by the temperature gradient is $I_T = I_{\bar{T}} + I_{T'}$, and the energy loss at the wall interface is I_W.

The influence of the thermodynamic effects was analyzed using the hydraulic losses and local entropy production rates, where EPRV and EPRT are the entropy production rates generated by the velocity and temperature gradients, respectively.

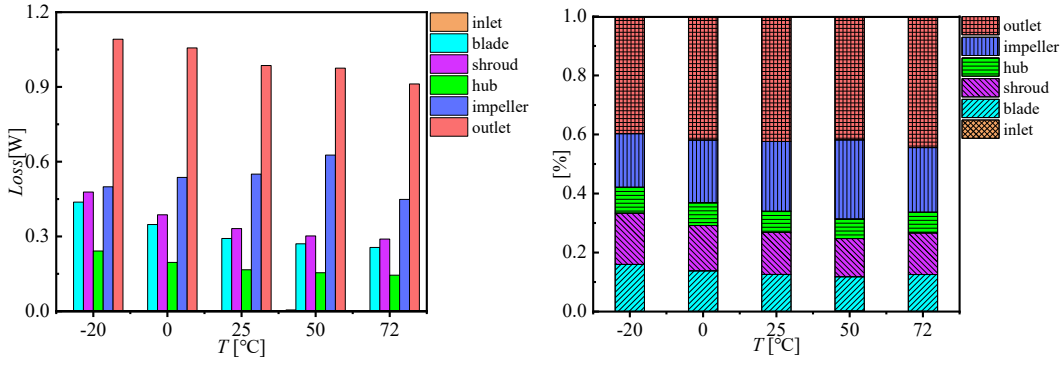


(a) σ = 0.01 (b) σ = 0.01

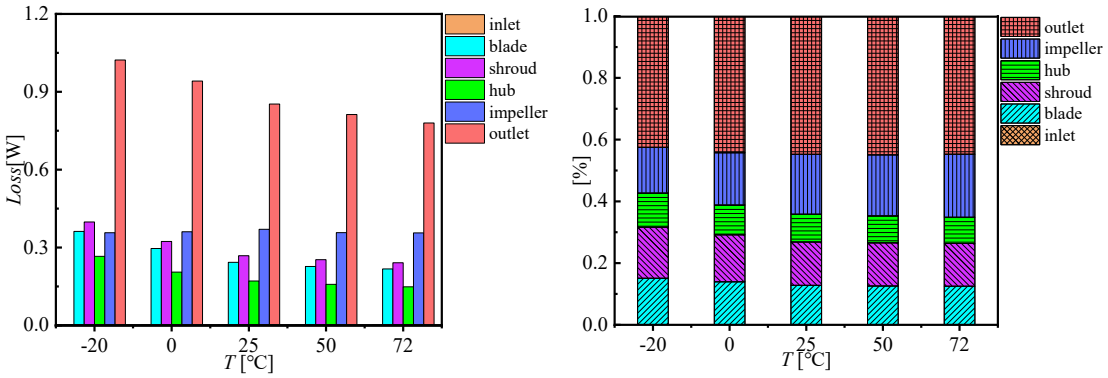
(c) σ = 0.2 (d) σ = 0.2

Fig. 10. Flow loss magnitude and proportion at different temperatures and cavitation numbers

Fig. 10 presents the magnitudes and proportions of various flow losses at different temperatures and cavitation numbers. Cavitation exacerbated flow loss. As shown in Fig. 10(a), under identical temperatures, the cavitating conditions exhibited significantly higher hydraulic losses than the non-cavitating conditions. This was evidenced by the increased I_D and I_W values, which resulted in an increase in the average total loss of approximately 20%. Specifically, I_D exhibited an average increase exceeding 20%, whereas I_W showed an average increase of approximately 13%. In addition, cavitation enhanced I_D dominance. As indicated in Fig. 10(a), increasing the temperature significantly suppressed the cavitation intensity through thermodynamic effects. Concurrently, the reduced viscosity diminished the wall shear stress and local velocity non-uniformity, leading to substantial reductions in flow losses. Consequently, both I_D and I_W were significantly reduced. Furthermore, cavitation significantly altered the composition of the lost components. The proportion of I_W decreased with increasing temperature. The magnitude of I_T was governed by the cavitation intensity. Thermodynamic effects suppressed cavitation development, consequently mitigating the temperature drop within the cavitation zones and reducing I_T. At 50°C, a sudden increase in the cavitation intensity amplified I_T.



(a) σ = 0.01 (b) σ = 0.01



(c) $\sigma = 0.2$ (d) $\sigma = 0.2$

Fig. 11. Losses and their proportions at different locations and temperature (σ = 0.2)

The outlet was consistently identified as the area with the most significant flow loss. A comparison of Figs. 11(a) and 11(c) reveals the minimal variation in the losses at this location because of its distance from the cavitation zones. The flow losses at the impeller exhibited a sudden surge with increasing cavitation intensity, with an average increase of approximately 40%; as seen at 50°C, a sharp rise of about 75% was observed. This abnormal increase in impeller losses at specific temperatures was closely correlated with the extremely high vapor volume fractions. At elevated temperatures, thermodynamic effects significantly suppressed cavitation and reduced impeller losses to near-noncavitating levels. Cavitation directly increased local losses, with the magnitude of this increase rising alongside the cavitation intensity. Losses in the blade and shroud regions were highly responsive to cavitation intensity variations, with the cavitation increasing by approximately 20%. On the blade-suction side, the cavitation cavities compressed the flow, augmented the local velocity gradients, and dissipated. Near the shroud, the accelerated vapor impingement on the wall surface intensified the wall losses.

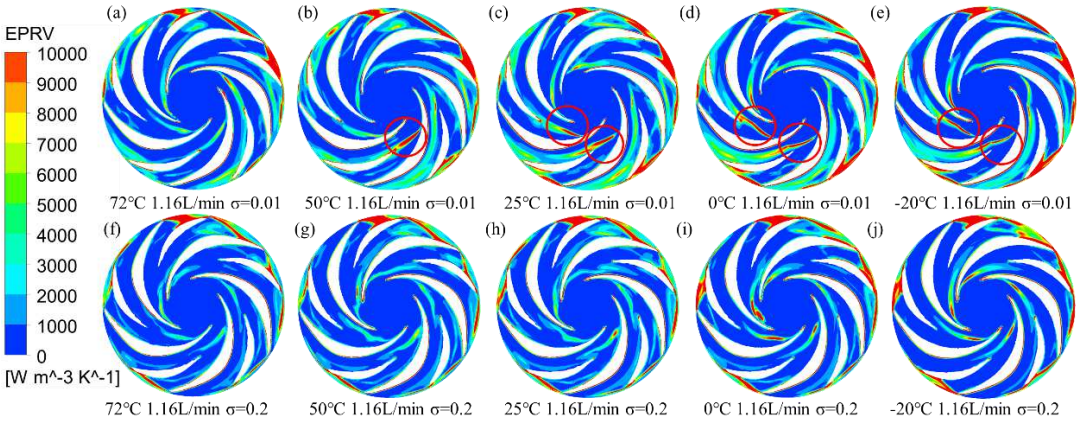


Fig. 12. Distribution of local EPRV at different temperatures (σ = 0.01)

High temperatures suppressed entropy production rates. A comparison of Figs. 12(f) and 12(j) reveals the significant reduction in regions of high EPRV (the entropy production rate generated by the velocity gradient) on the suction side of the long blade at 72°C versus -20°C. Increasing the temperature lowered the fluid viscosity, resulting in more uniform local velocity distributions, and consequently, reduced energy dissipation. Cavitation significantly intensified the EPRV in high-EPRV regions. A comparison of Figs. 12(e) and 12(j) reveals that cavitation elongated the high EPRV banded zones in the areas of peak cavitation intensity. At low cavitation numbers, the high-EPRV region at the periphery of the impeller also exhibited significant expansion. A comparison of Figs. 12(a) and 12(f) demonstrates that elevated temperatures suppressed the cavitation intensity through thermodynamic effects, reducing the EPRV on the suction side of the long blade to near-non-cavitating levels. The increased temperature curbed the enhancement effect of cavitation on the local EPRV.

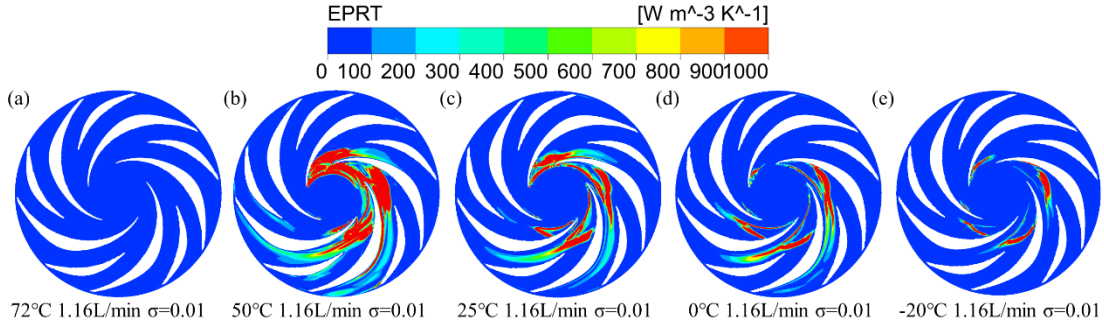


Fig. 13. Distribution of local EPRT at different temperatures (σ = 0.01)

As shown in Fig. 13(e), the high EPRT (entropy production rate generated by the temperature-gradient) area at low temperatures was mainly concentrated in the region where vapor condensation occurs at the tail edge of the bubble. As shown in Figures 13(c) and (d), as the temperature increased, the high-EPRT area gradually expanded towards the interior of the bubble and the downstream area of cavitation. As evident from Fig. 13(b), owing to the thermodynamic effect, it did not occur simultaneously with the temperature change. At 50℃, the high EPRT area was widely distributed within the cavitation region, and at this time, the overall vapor volume fraction decreased. As shown in Fig. 13(a), the thermodynamic effects dominated, significantly inhibiting the cavitation process, and the overall EPRT decreased rapidly.

As shown in Fig. 13(e), at low temperatures, the high-EPRT regions were predominantly clustered near the cavitation-cavity trailing edges, where vapor condensation induced intense temperature gradients. Figs. 13(c) and (d) show that as the cavitation intensified, the high EPRT zones progressively extended toward the cavity interior and downstream regions. As evident in Figure 13(b), due to the fact that the inhibitory effect of thermodynamic effects on cavitation was not synchronized with the temperature changes, the overall steam volume fraction decreased at 50℃, resulting in the widespread distribution of a high EPRT area. As shown in Figure 13(a), the thermodynamic effect dominated, significantly suppressing the development of cavitation, and the EPRT level rapidly decreased.

4. Conclusions

A numerical study was conducted on the cavitation flow of an entire space micropump considering the thermodynamic effects. The ZGB cavitation model was modified, and a multiphase simulation method was used to simulate the cavitation of the PFTEA in the space micropump. The influence of thermal effects on cavitation flow was studied in terms of the internal flow field, cavity morphology, and hydraulic loss. The results show that:

(1) Cavitation degrades the performance of the micropump, leading to a reduction in head, an increase in shaft power, and a significant decline in efficiency. However, an increase in the temperature mitigates these adverse effects by suppressing cavitation.

(2) The temperature variation influences cavitation by altering the saturated vapor pressure, viscosity, and thermodynamic effects of the liquid. At lower temperatures, the cavitation area is dispersed with larger irregular cavitation cavities. Elevated temperatures inhibit cavitation, reduce the cavity size, and diminish the vapor volume fraction. However, the suppressing effect of the thermodynamic mechanisms does not scale proportionally with the temperature increase.

(3) Cavitation enhances the local flow inhomogeneity, turbulent dissipation, and flow losses, and this is accompanied by an increased local entropy generation rate. Furthermore, an increase in temperature reduces flow losses by suppressing cavitation and reducing the liquid viscosity.

The cavitation flow of PFTEA over a wide temperature range significantly affects the performance characteristics and safety of space micropumps. As such, the problems caused by cavitation in space micropumps require a more thorough understanding. The instability of space micropumps can be further studied using more precise numerical simulations and abundant experimental data.

Conflict of Interests

The authors declare that there is no conflict of interests regarding the publication of this article.

Credit Author Statement

Chuanchao, Wang: Methodology, Formal analysis, Writing – original draft, Writing – review & editing, Deyou, Li: Writing – original draft, Writing – review & editing, Resources, Funding acquisition, Project administration, Software, Qi Yang: Writing –review & editing, Zhiwei Liu: Writing–review & editing, Xiaolong Fu: Writing– review & editing, Jintao, Liu: Writing – review & editing, Zhipeng Ren: Writing – review & editing.

Acknowledgement

The authors would like to thank Fundamental Research Funds for the Central Universities (No. FRFCU5710052422)), for their financial supports.

Data Availability

The ANSYS Fluent case files and processed data are available from the corresponding author upon reasonable request.

Ethics Approval

Not applicable.

References

[1] Li D, Ren Z, Li Y, et al. Thermodynamic effects on the cavitation flow of a liquid oxygen turbopump[J]. Cryogenics, 2021,116(6):103302.

[2] Pace G, Valentini D, D'Agostino H. Analysis of flow instabilities on a three-bladed axial inducer in fixed and rotating frames[J]. Journal of Fluids Engineering: Transactions of the ASME, 2019,141(4):41101-41104.

[3] Hosangadi A, Ahuja V. Numerical study of cavitation in cryogenic Fluids[J]. Journal of Fluids Engineering, 2005,127(2).

[4] Pan H, Li Y, Zhuang B, et al. Spacecraft fluid management and control[M]. Beijing: China Astronautic Publishing House, 2020(in Chinese).

[5] Tan L, Zhu B, Cao S, et al. Cavitation flow simulation for a centrifugal pump at a low flow rate[J]. Chinese Science Bulletin, 2013,58(8):949-952.

[6] Sun W, Tan L. Cavitation-vortex-pressure fluctuation interaction in a centrifugal pump using bubble rotation modified cavitation model under partial load[J]. Journal of Fluids Engineering: Transactions of the ASME, 2020(5):142.

[7] Mousmoulis G, Karlsen-Davies N, Aggidis G, et al. Experimental analysis of the onset and development of cavitation in a centrifugal pump[J]. Journal of Physics Conference, 2017,813(1):12044.

[8] Wang J, Wang Y, Liu H, et al. Rotating corrected based cavitation model for a centrifugal pump[J]. Journal of Fluids Engineering, 2018,140(11):111301.

[9] Jia X, Zhang Y, Lv H, et al. Study on external performance and internal flow characteristics in a centrifugal pump under different degrees of cavitation[J]. Physics of Fluids, 2023,35(1):-.

[10] Rakibuzzaman M, Park N, Suh S. Analysis of cavitation with rotational speed and water temperature changes of centrifugal pump[J]. The KSFM Journal of Fluid Machinery, 2017,20(5).

[11] Zhang B, Niu B, Zhang Z, et al. Application and challenge of high-speed pumps with low-Temperature Thermosensitive Fluids[J]. Energies, 2024,17.

[12] Zhang Z, Yang S, Zhang B, et al. Experimental study on hydraulic performance and cavitation characteristics of a R134a refrigerant self-lubricating centrifugal pump[J]. International Journal of Refrigeration, 2025,169:204-213.

[13] Liu Q, Qi X, Zhu Z, et al. Investigation of cavitation characteristics in an aircraft centrifugal fuel pump[J]. Flow Measurement and Instrumentation, 2024:96.

[14] Yao Z, Luo X, Ji B, et al. A Thermodynamic cavitation model for cavitating flow simulation in a wide range of water temperatures[J]. Chinese Physics Letters, 2010,27(1):4.

[15] Xu B, Liu K, Deng Y, et al. The characteristics of unsteady cavitation around a NACA0015 hydrofoil with emphasis on the thermodynamic effect[J]. Ocean Engineering, 2022.

[16] Tian H.Investigation on characteristics of cavitating flow and thermodynamic effects in high temperature water[D]. Xi'an: Xi'an University of Technology, 2023(in Chinese).

[17] Sunjae K ,Nishad D ,Issam M , et al.Cryogenic flow boiling in microgravity: Effects of reduced gravity on two-phase fluid physics and heat transfer[J].International Journal of Heat and Mass Transfer,2024,218 :124751.

[18] Agarwal R ,Dondapati S R .Numerical investigation on hydrodynamic characteristics of two-phase flow with liquid hydrogen through cryogenic feed lines at terrestrial and microgravity[J].Applied Thermal Engineering,2020,173(prepublish):115240.

[19] Zhu Z, Wang Y, Liu Q, et al. Effect of Bond number variation on contact angle of droplet on solid wall[J]. Journal of Engineering Thermophysics, 2012, 33(2): 251-254(in Chinese).

[20] Mousavi S, Lee B. Investigation of bubble structure in a microchannel under microgravity conditions: Effects of discontinuous wettability with dynamic contact angle[J]. Acta astronautica, 2022.

[21] Kikuta K. Thermodynamic effect on cavitation performances and cavitation instabilities in an inducer[J]. ASME, Jounal of Fluids Engineering, 2008,130.

[22] Li D, Wang H, Qin Y, et al. Entropy production analysis of hysteresis characteristic of a pump-turbine model[J]. Energy Conversion and Management, 2017,149(oct.):175-191.

[23] Li D, Miao B, Li Y, et al. Numerical study of the hydrofoil cavitation flow with thermodynamic effects[J]. Renewable Energy, 2021,169(9).

[24] Yu A, Tang Q, Zhou D, et al. Entropy production analysis in two-phase cavitation flows with thermodynamic cavitation model[J]. Applied Thermal Engineering, 2020,171:115099.

[25] Wang X , Wang Y , Liu H ,et al.A numerical investigation on energy characteristics of centrifugal pump for cavitation flow using entropy production theory[J].International Journal of Heat and Mass Transfer, 2023.

[26] Lai F, Huang M, Wu X, et al. Local entropy generation analysis for cavitation flow within a centrifugal pump[J]. Journal of Fluids Engineering, 2022.

[27] Li Y, Lai H. Numerical analysis of cavitation flow in micro high-speed pump[J]. Journal of East China University of Science and Technology (Natural Science Edition), 2016, 42(1): 8(in Chinese).

[28] Menter F. Two-equation eddy-viscosity turbulence models for engineering applications[J]. Aiaa Journal,1994,32(8):1598-1605.

[29] Moore R D, Ruggeri R S. Method for prediction of pump cavitation performance forvarious liquids, liquid temperatures, and rotative speeds[J], 1969.

[30] Franc J-P, Rebattet C, Coulon A. An Experimental Investigation of Thermal Effects in a Cavitating Inducer[J]. Journal of Fluids Engineering, 2004, 126(5):7

Supplementary Files

This is a list of supplementary files associated with this preprint. Click to download.

- Highlights.docx